Research Article Vol. 31, No. 24 / 20 Nov 2023 / Optics Express 40070
Optics EXPRESS

Method for retrieval of aerosol optical depth from multichannel irradiance measurements

MILOS SZTIPANOV,[1,*] WEI LI,[1] ARNE DAHLBACK,[2] JAKOB STAMNES,[3] TOVE SVENDBY,[4] AND KNUT STAMNES[1]

[1]Department of Physics, Stevens Institute of Technology, Hoboken, New Jersey, USA
[2]University of Oslo, Oslo, Norway
[3]University of Bergen, Bergen, Norway
[4]Norwegian Institute of Air Research, Kjeller, Norway
[*]milostipanov@gmail.com

Abstract: We present, to the best of our knowledge, a new method for retrieval of aerosol optical depth from multichannel irradiance measurements. A radiative transfer model is used to simulate measurements to create the new aerosol optical depth retrieval method. A description of the algorithm, simulations, proof of principle, merits, possible future developments and implementations is provided. As a demonstration, measurements in the New York City area are simulated based on the specific channel configuration of an existing multichannel irradiance instrument. Verification of the method with irradiance measurement data is also provided.

© 2023 Optica Publishing Group under the terms of the Optica Open Access Publishing Agreement

1. Introduction

Aerosols influence the transfer of radiation in the atmosphere, the climate system, the biosphere, and human health. Aerosols absorb and scatter light, modify clouds, influence the global radiative energy balance and transport chemicals. Globally, exposure to particulate matter from fossil fuel emissions accounted for 21.5% of total deaths in 2012, and 18% in 2018 [1]. Recently aerosols have received attention in regard to transmission of the SARS-CoV-2 virus [2,3]. For these reasons monitoring aerosol properties and abundance is important. Aerosols come in different compositions, sizes, and shapes that affect their optical properties. The aerosol quantity determined by most instruments is the aerosol optical depth (AOD). A considerable effort has been put into developing instruments, sensors and algorithms to quantify AOD [4].

The aim of this article is to provide a flexible, simple algorithm for AOD retrieval under cloud-free sky conditions, from ground-based irradiance measurements, that can also be easily applied, improved and customized to the circumstances of a given measurement and instrument. The described method can also be applied to analyze data from instruments deployed on aircraft. The wavelength channels of a NILU-UV (Norwegian Institute for Air Research - Ultraviolet) instrument [5] will be used for demonstration purposes, and aerosol properties will be assumed to be similar to those typically present in cities and urban areas. As discussed in Section 7 the methodology described in this paper can readily be applied to a number of different irradiance instruments that have been deployed in a multitude of campaigns by NASA and NOAA.

In summary, the AOD retrieval method includes the following four main steps: (i) taking irradiance measurements with a multichannel irradiance instrument; (ii) carrying out radiative transfer simulations for the measurement configuration and for a variety of aerosol amounts (volume fractions); (iii) taking the ratio of the simulated irradiances at two different wavelengths, and (iv) comparing the simulated ratio to a measured ratio at the same wavelengths. A detailed description of each step of the algorithm is provided.

#493712 https://doi.org/10.1364/OE.493712
Journal © 2023 Received 20 Apr 2023; revised 12 Jul 2023; accepted 12 Jul 2023; published 10 Nov 2023

Optics EXPRESS

2. Motivation

Currently one of the largest aerosol optical depth retrieval networks is the AErosol RObotic NETwork or AERONET, which uses measurements recorded by the CIMEL CE318-T instrument family for AOD retrievals [6]. A preprogrammed sequence of either direct sun or sky, measurements is taken by the CIMEL instrument, which has nine interference filters at wavelengths 340, 380, 440, 500, 670, 870, 940, 1020, and 1640 nm. These are placed in a filter wheel which is rotated by a stepping motor to enable radiance measurements at the nine different wavelengths. The accuracy of the spectral AOD measured by direct sun observations with Level 2 data for overhead sun ranges from $\sim$ 1% in the visible and near-infrared to $\sim$ 2% in the UV radiation [7]. The AERONET AOD data from direct sun observations are widely utilized by the scientific community. The optical depth is calculated from the extinction of the direct beam irradiance at each wavelength based on the Beer-Bouguer Law. Attenuation due to Rayleigh scattering, and absorption by ozone, and trace gases are estimated and removed to isolate the attenuation due to aerosols, i.e., the aerosol optical depth. A sequence of three such measurements are taken 30 seconds apart creating a triplet observation per wavelength.

The inversion method of the AERONET [8] is based on several assumptions and constraints and relies on separate measurements to determine several aerosol parameters, such as size distribution and the complex refractive index, which are used to compute the aerosol scattering phase function and the single-scattering albedo as well as spectral and broadband irradiances. The retrieval provides estimates of effective radius [see Eq. (5)], standard deviation, and volume concentrations for both fine and coarse modes of the retrieved size distribution. Surface reflectance is modeled. The single-scattering albedo of the fine- and coarse-mode aerosol particles is estimated. The AERONET retrieval is implemented under the assumption that the complex refractive index is the same for all particle sizes. Gaseous absorption by ozone, nitrogen dioxide, and water vapor is accounted for in the inversion method. The total column water vapor amount is determined from the 940 nm channel measurements. The total ozone optical depth is determined utilizing the total column TOMS (Total Ozone Mapping Spectrometer) monthly average climatology. Similarly, the nitrogen dioxide (NO_2) optical depth is calculated using the total column OMI (Ozone Monitoring Instrument) monthly average climatology (2004-2013) of the NO_2 concentration.

As described above, the CIMEL instruments have several moving parts and rely on preprogrammed measurement sequences (depending on the location) that are time-consuming and make them unsuitable for as frequent data acquisition as NILU-UV's. The direct sun AOD measurements are made at 5 minute intervals while the NILU-UV instrument takes measurements at 1 second intervals. An absolute calibration of the CIMEL instrument needs to be done at the calibration facility every 6-12 month. With casing the instrument weighs 30 kg so transportation can be more costly and impractical as compared to the NILU-UV. More information about AERONET can be found at https://aeronet.gsfc.nasa.gov.

The challenges and practical limitations associated with CIMEL measurements motivate the search for a robust, effective, yet reliable method for AOD retrieval based on measurements obtained by simple irradiance meters with no moving parts. The algorithm described in this paper can also be applied to measurements taken by devices such as the Solar Spectral Flux Radiometer (SSFR) instrument. The SSFR is a well-characterized irradiance sensor with a wavelength range of 350 nm to 2150 nm, a spectral resolution of $\sim 8-12$ nm and a long flight heritage. It was deployed in numerous missions, to name a few: FIRE III Arctic Cloud Experiment (FIRE-ACE), 1998 [9]; ERAST/ARM UAV Kauai Experiment, 1999; DOE Atmospheric Radiation Measurement (ARM) Enhanced Shortwave Experiment (ARESEII), 2000; Puerto Rico Dust Experiment (PRIDE), 2000 [10]; Southern African Regional Science Initiative (SAFARI), 2000 [11]; the Asian Pacific Regional Aerosol Characterization Experiment (ACE-Asia), 2001 [12]; the Cirrus Regional Study of Tropical Anvils and Cirrus Layers - Florida Area Cirrus Experiment (CRYSTAL-FACE), 2002 [13]; the ARM UAV Fall 2002 Experiment; the 2003 DOE ARM Aerosol IOP, the Intercontinental

Optics EXPRESS

Chemical Transport Experiment - North America (INTEX-NA), 2004 [14]; the Mixed - Phase Arctic Cloud Experiment (MPACE), 2004; the Megacity Initiative: Local and Global Research Observations (MILAGRO), 2006 [15]; the Gulf of Mexico Atmospheric Composition and Climate Study (GoMACCS), 2006 [16,17]; the PACific Dust4 Experiment (PACDEX), 2007 [18]; the Tropical Composition, Cloud and Climate Coupling (TC4) mission, 2007; the Arctic Research of the Composition of the Troposphere from Aircraft and Satellites (ARCTAS), 2008 [19]; the Aerosol, Radiation, and Cloud Processes affecting Arctic Climate (ARCPAC) experiment, 2008 [20], and the CalNex experiment in 2010 [21].

In addition, the SSFR instrument has been deployed on numerous aircraft, on the ground, and on research vessels.

3. Simulating radiative transfer using AccuRT

AccuRT (Accurate Radiative Transfer) is a unique, state of the art radiative transfer simulation package that was designed to provide a reliable, well-tested, robust, versatile, and easy-to-use radiation transfer tool for coupled (atmosphere and underlying surface) systems [22]. For demonstration purposes and to make the approach more tangible, irradiances were simulated at two wavelengths, 340 nm and 380 nm, for a measurement configuration involving a NILU-UV irradiance meter [5].

Use of the aerosol volume fraction, f_V, to quantify the aerosol amount in the atmosphere is practical because while the AOD is wavelength dependent, f_V is not. In our simulations we will change the AOD values by varying the aerosol volume fraction, f_V. The retrieved AOD value at a given wavelength, will be determined based on f_V, defined as [23]

$$f_V = \int_{r_{min}}^{r_{max}} \frac{4\pi}{3} r^3 n(r) dr \tag{1}$$

where $n(r)$ is the aerosol size distribution in terms of number density. According to Eq. (1), f_V is simply the volume fraction of an air parcel occupied by aerosol particles. A bimodal, log-normal size distribution is frequently adopted to represent atmospheric aerosols [24]

$$n(r) = \frac{dN(r)}{dr} = \frac{dN(r)}{d(\ln r)} = \sum_{i=1}^{2} \frac{N_i}{\sqrt{2\pi}\sigma_i} \exp\left[-\left(\frac{\ln r - \ln r_{n,i}}{\sqrt{2}\sigma_i}\right)^2\right] \tag{2}$$

where N_i is the total number of particles of mode i, $r_{n,i}$ is the mean geometric (or mode) radius, and σ_i is the geometric standard deviation. In terms of volumes Eq. (2) becomes:

$$v(r) = \frac{dV(r)}{dr} = \frac{dV(r)}{d(\ln r)} = \sum_{i=1}^{2} \frac{V_i}{\sqrt{2\pi}\sigma_i} \exp\left[-\left(\frac{\ln r - \ln r_{n,i}}{\sqrt{2}\sigma_i}\right)^2\right] \tag{3}$$

where the summation is over $i = 1 = f$ (fine mode) and $i = 2 = c$ (coarse mode).

The bimodal distribution [Eq. (3)] adopted for our instrument location can be thought of as being composed of one mode consisting of small (potentially absorbing) particles of continental origin and the other mode consisting of large, hygroscopic, non-absorbing particles of maritime origin. The two modes are frequently referred to as the fine mode occupying volume V_f and the coarse mode occupying volume V_c, so that $V_f + V_c = V$ is the total volume occupied by aerosol particles. In general there is a wide range of aerosol types and their microphysical and optical properties for each mode. In this paper we will often refer to the fine and coarse modes as urban and maritime modes receptively, as these are the aerosol types relevant to our measurement location. A volume size distribution is plotted (based on Eq. (3)) in Fig. 1 with volume geometric mean (mode) radii: 0.1499 μm, $r_{n,c}$ = 2.1786 μm and σ_f = 0.437, σ_c = 0.672 as geometric standard deviations. These values are also used in Sections 4, 5, 6, and 7 The distribution is

Optics EXPRESS

normalized to $\int_0^\infty v(r)dr = V_f + V_c = V = 1$ with $V_f = V_c = 0.5$. The mode radii $r_{n,f}$ and $r_{n,c}$ are indicated in Fig. 1.

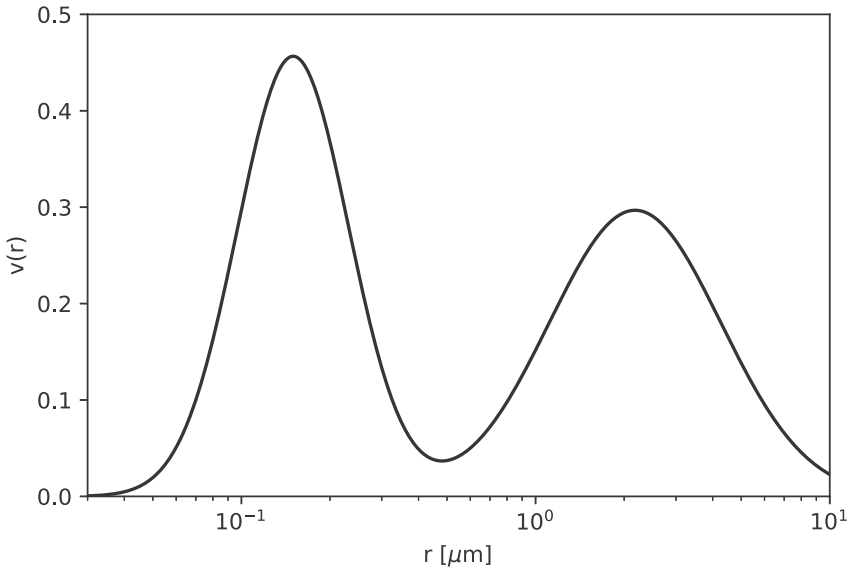

Fig. 1. A bimodal, log-normal aerosol volume size distribution (used in later sections) with mode radii $r_{n,f} = 0.1499$ μm, $r_{n,c} = 2.1786$ μm and $\sigma_f = 0.437$, and $\sigma_c = 0.672$ as geometric standard deviations.

The fine-mode volume fraction, defined as the fraction of the total volume of the aerosol particles occupied by fine-mode particles, denoted with f_f [not to be confused with f_V, the total volume fraction of aerosol particles contained in an air parcel, see Eq. (1)], is given by:

$$f_f = \frac{V_f}{V_f + V_c} = \frac{V_f}{V}. \tag{4}$$

In addition to the mode radius $r_{n,i}$ ($i = f$ or $i = c$) appearing in Eq. (2), the particle size distribution can also be characterized by an effective mode radius [23].

$$r_{\text{eff},i} = \frac{\int_{r_{min}}^{r_{max}} n(r) r_{n,i}^3 dr}{\int_{r_{min}}^{r_{max}} n(r) r_{n,i}^2 dr}. \tag{5}$$

For a log-normal size distribution the two radii are related by

$$r_{\text{eff},i} = r_{n,i} \exp(2.5\sigma_i^2). \tag{6}$$

As shown in Fig. 1, two mono-modal size distributions are combined to create a bimodal size distribution with a fine mode that describes aerosols in urban areas and a coarse mode that is typical for aerosols in open ocean areas or maritime environments. Such a bimodal size distribution of aerosols is often found near cities in coastal areas. The parameters of the bimodal size distribution are provided in Section 6. In this study (unless otherwise indicated) the fine- and coarse-mode volume fractions are set to $f_f = 0.5$ and $f_c = 1 - f_f = 0.5$, respectively. In Section 6 we explore how the retrieved aerosol optical depth would depend on our choice of the fine/coarse mode aerosol volume fractions. The aerosol particles are assumed to be located in the troposphere between 0 and 2000 m (i.e., from sea level up to 2000 m altitude). For the

Optics EXPRESS

radiative transfer simulations we used two sets of complex refractive indices. One was chosen to represent typical fine-mode aerosols (anthropogenic, water-soluble particles) and another to represent coarse mode aerosols (sea salt, minerals). The real and imaginary parts of the refractive index for different wavelengths of the fine- and coarse-mode aerosols were adopted from [24] and [22]. A list of refractive indices is provided in Table 1.

Table 1. The complex refractive index values ($m = m_r + im_i$) used for the fine and coarse modes of the aerosol particles.[a]

wavelength	fine mode		coarse mode	
λ [nm]	m_r	m_i	m_r	m_i
337.1	1.53110	0.010253	1.510	4×10^{-7}
412	1.53110	0.010253	1.500	10^{-7}
443	1.53110	0.010236	1.500	10^{-7}
490	1.53110	0.010210	1.500	10^{-7}
514.5	1.53110	0.010210	1.500	10^{-8}
555	1.53110	0.010157	1.499	10^{-7}
632.8	1.53110	0.010110	1.500	2×10^{-8}
670	1.53110	0.010110	1.490	10^{-7}
860	1.52115	0.010110	1.480	3×10^{-6}
869	1.52110	0.010112	1.480	3×10^{-6}
1069	1.52115	0.010160	1.470	2×10^{-4}

[a]The real part m_r is related to the phase velocity of light and the imaginary part to the absorption coefficient.

Unless otherwise indicated the US standard atmosphere model was used in the simulations (for details see [22]). The surface was assumed to be a Lambertian reflector with an albedo of 0.14, that is typical for cities [25]. The instrument detection altitude was set to 40 m above the sea level to mimic a typical measurement configuration for the location of the instrument used in this study for demonstration purposes (see Sections 4 and 8). The basic setup described above, will be used for our measurement simulations described in the next section to investigate the retrieval of the AOD.

4. Measurement simulations and aerosol optical depth retrieval

Assuming that the aerosols are spherical particles and that we have computed the inherent optical properties (IOPs) for particles with a specified refractive index and a variety of sizes, we may compute the absorption coefficient $\alpha_p(\lambda)$, the scattering coefficient $\beta_p(\lambda)$, and the scattering phase function $p_p(\lambda, \theta)$ for a polydispersion of particles by integrating over the size distribution $n(r)$:

$$\alpha_p(\lambda) = \int_{r_{min}}^{r_{max}} \pi r^2 Q'_\alpha(r) n(r) dr \tag{7}$$

$$\beta_p(\lambda) = \int_{r_{min}}^{r_{max}} \pi r^2 Q'_\beta(r) n(r) dr \tag{8}$$

$$p_p(\lambda, \theta) = \frac{\int_{r_{min}}^{r_{max}} p_p(\lambda, \theta, r) n(r) dr}{\int_{r_{min}}^{r_{max}} n(r) dr}. \tag{9}$$

Optics EXPRESS

In Eqs. (7) and (8) $Q'_\alpha(r)$ and $Q'_\beta(r)$ are the absorption and scattering efficiencies, respectively, where 'efficiency' is defined as the ratio of the optically active cross section to the geometrical cross section πr^2 of the spherical particle.

The user specifies the location (altitude profile) of the aerosols as well as the refractive indices of the fine and coarse particle modes, the effective radii $r_{\text{eff},f}$ and $r_{\text{eff},c}$ (see Eq. (5)), geometric standard deviations σ_f and σ_c and the fine mode volume fraction f_f (see Eq. (4)). AccuRT uses a Mie code to compute the IOPs of aerosol particles [$Q'_\alpha(r)$, $Q'_\beta(r)$ and $p_p(\lambda, \theta, r)$ in Eqs. (7)–(9), and integration over the log-normal size distributions is performed numerically to obtain $\alpha_p(\lambda)$, $\beta_p(\lambda)$ and $p_p(\lambda, \theta)$ [22].

In our study, the two wavelengths used correspond to those of channel 4 (340 nm) and channel 5 (380 nm) of a NILU-UV irradiance instrument. The aerosol volume fraction range was adopted to be $f_V \in [0, 10^{-10}]$, with 30 equidistant sampling points. For a coarse mode size distribution ($f_c = 1$), representing aerosols for a maritime environment, the proportionality between f_V and the AOD, is clearly demonstrated in Fig. 2 at 340 nm and at 500 nm. AOD is often measured at 500 nm, hence the added AOD at this wavelength. In section 8, AOD at this same wavelength will be used to compare results to AERONET. The same simulation was done for an urban size distribution, using $f_c = 0$, see Fig. 3. To obtain a finer AOD and aerosol volume fraction (f_V) resolution, one can use more data points in the f_V range.

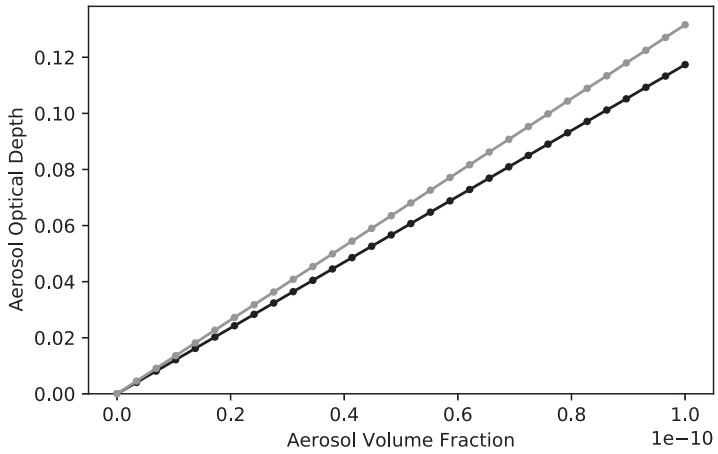

Fig. 2. Simulated AOD at 340 nm (black) and 500 nm (gray) vs. aerosol volume fraction, f_V for maritime size distribution.

If we want to retrieve AOD values for different wavelengths we can use the same or an adjusted f_V range as input to obtain the corresponding AOD values from AccuRT simulations. This approach speeds up the computations and reduces the possibility of calculation errors.

The steps required to retrieve the AOD are:

1. Generate lookup-table: Run AccuRT to simulate the measurements for a range of f_V values [f_{Vmin},f_{Vmax}] corresponding to a range of AOD values (see Figs. 2 and 3). Additional inputs for the AccuRT simulations are solar zenith angle range [$\theta_{0,\text{min}}, \theta_{0,\text{max}}$], and aerosol parameters (complex refractive indices of the fine and coarse mode, effective radii, variances, and fine mode fraction).

2. Take the ratio of measured irradiances from two channels of a multichannel irradiance meter at the time of interest $\left(\frac{F'_i}{F'_j}\right)$.

3. Take the ratio of the simulated irradiances $\left(\frac{F_i}{F_j}\right)$.

Optics EXPRESS

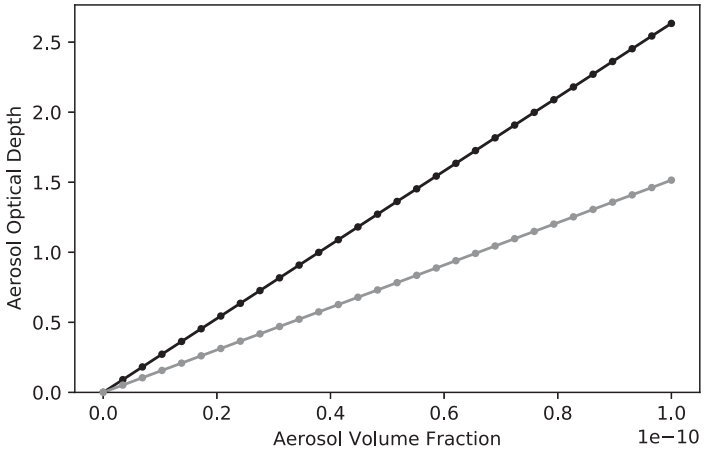

Fig. 3. Simulated AOD at 340 nm (black) and 500 nm (gray) vs. aerosol volume fraction, f_V for a urban size distribution.

4. Search for the nearest match of the measured $\left(\frac{F_i'}{F_j'}\right)$ ratio in the simulated dataset to determine the corresponding AOD value. Hence, search for $\frac{F_i}{F_j}$, when $\left|\frac{F_i'}{F_j'} - \frac{F_i}{F_j}\right|$ is at minimum.

A schematic illustration of the method is provided in Fig. 4.

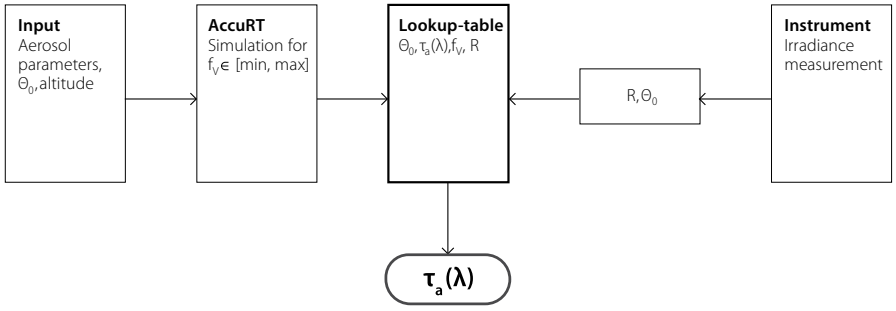

Fig. 4. Schematic illustration of the algorithm for retrieving the AOD ($\tau_a(\lambda)$ at solar zenith angle θ_0. The ratio R is defined in Eq. (15)

Use of two channels is sufficient to determine the f_V value, which through further simulations can be used to determine the AOD at different wavelengths assuming that the same atmospheric conditions apply. The retrieved total AOD value depends on the fine/coarse aerosol mode ratio f_f/f_c, which is investigated in Section 6. AccuRT is capable of separating the AOD for the two different (fine and coarse) aerosol modes, but in this study our focus is on determining the AOD.

The most time-consuming part of the retrieval algorithm described in steps 1–4 above is setting up and running the simulations for the possible measurement configurations. As is clear from Figs. 2 and 3, a wide range of AOD values can be covered with 30 sampling points, which provides AOD values at steps of $\Delta\tau_a(\lambda = 340\text{ nm}) = 0.004$ using the size distribution for maritime aerosols and $\Delta\tau_a(\lambda = 340\text{ nm}) = 0.09$ using the size distribution for urban aerosols. Values of τ_a can be linearly interpolated for f_V values between the grid points.

On our hardware (2x 4-Core Xeon E5335 2.0 GHz, 8 Clovertown Cores, 20 GB System Memory) computational time for running a simulation with such precision for the possible solar zenith angles at our location with increments of $\Delta\theta = 1$ and for the two wavelengths is in the

Optics EXPRESS

magnitude of hours. The time needed to retrieve an AOD value from the pre-computed look-up tables is negligible. Therefore, for a measurement scenario of interest this algorithm provides an efficient method for AOD retrieval.

5. Proof of principle

In order to prove that the method described above will work we need to show that the ratio of the irradiances for the two channels (340 and 380 nm) is indeed sensitive to the volume fraction of aerosols f_V. The output of the model described in Section 2 provides the desired AOD values and corresponding irradiance values $F(\lambda)$, so that the ratio

$$R = F(340\ \text{nm})/F(380\ \text{nm}) \tag{10}$$

can easily be calculated for various AOD values. As demonstrated in Section 7 the 340 nm channel is not, and the 380 nm channel is scarcely sensitive to the ozone abundance in the atmosphere. The results are illustrated in Fig. 5.

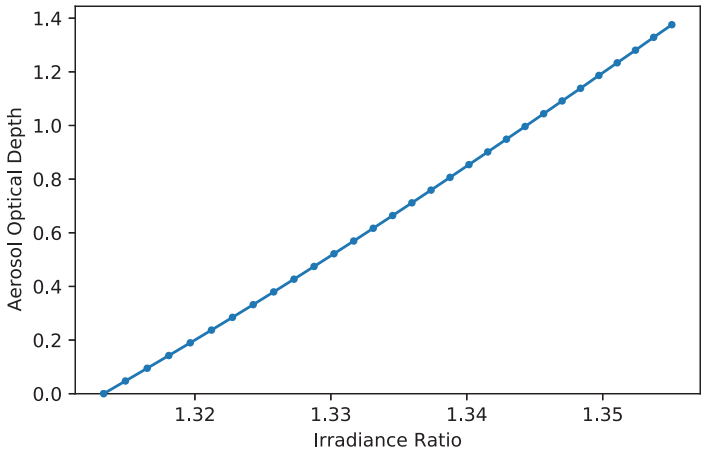

Fig. 5. Aerosol optical depth (AOD) at 340 nm versus the irradiance ratio $F(340\ \text{nm})/F(380\ \text{nm})$ for a bimodal size distribution with fine-mode fraction $f_f = 0.5$.

6. Sensitivity to the fine- and coarse-mode volume fractions

In this Section we investigate how sensitive the aerosol optical depth (AOD) would be to the fine- and coarse-mode aerosol volume fractions f_f and f_c adopted in the simulations. The first set of simulations were conducted for three different aerosol fine-mode fractions, f_f, see Eq. (4), at three different aerosol volume fractions, f_V, see Eq. (1) for the measurement configuration described in Section 3.

We used an aerosol particle size distribution [24] with values for the maritime aerosol case given by mean radii for the fine and coarse modes as $r_{n,f} = 0.1499\ \mu$m and $r_{n,c} = 2.1789\ \mu$m, respectively with standard deviations of $\sigma_f = 0.437$ and $\sigma_c = 0.672$. As expected, the closer the mean radii of the fine and coarse particle modes, the less the sensitivity of the AOD to the mode fractions f_f and f_c. This size distribution is a good option to assess the sensitivity under this extreme condition. As mentioned in Section 4 the fine mode represents urban-like (potentially absorbing) aerosols, while the coarse mode represents the properties of maritime aerosols. This combination of urban and maritime aerosols is common in a coastal city environment, such as that at our measurement site (see Section 8).

Optics EXPRESS

To span the previously defined volume fraction range ($f_V \in [0, 10^{-10}]$), we chose the following three aerosol volume fractions: $f_{V_1} = 3.448 \cdot 10^{-12}$, $f_{V_2} = 3.448 \cdot 10^{-11}$ and $f_{V_3} = 10^{-10}$. For each of these volume fractions, three different cases were considered with $f_f = 0$, $f_f = 0.5$, and $f_f = 1$, representing scenarios in which the atmosphere consists of respectively (i) only coarse-mode aerosols, (ii) equal volume fractions of fine- and coarse-mode aerosols, and (iii) only fine-mode aerosols. The outcome of these simulations is shown in Fig. 6.

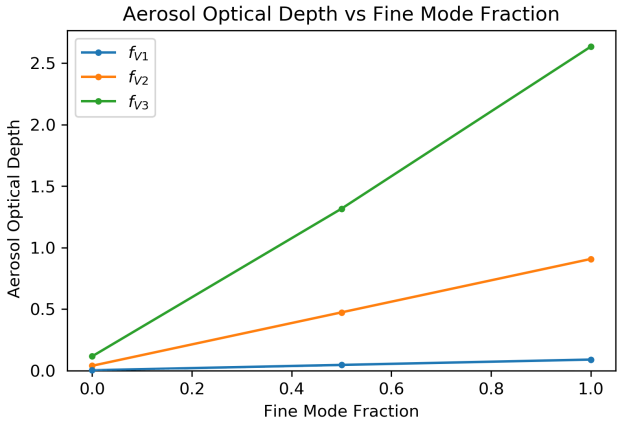

Fig. 6. Aerosol optical depth at 340 nm vs. fine-mode fraction for three different aerosol volume fractions: $f_{V_1} = 3.448 \cdot 10^{-12}$, $f_{V_2} = 3.448 \cdot 10^{-11}$ and $f_{V_3} = 10^{-10}$.

Figure 6 shows that fine-mode aerosols of the bimodal size distribution contribute significantly to the AOD at 340 nm. Thus, as the fine-mode fraction increases the AOD increases as well. The simulations in Fig. 6 show that at $f_f = 0.5$, fine-mode aerosols contribute 95% to the total AOD. At such locations, the main contribution to the total AOD comes from fine-mode aerosols, such as fine dust and soot, and in smaller amounts from other water-soluble polluting particles.

As shown in Fig. 6, the impact of different fine-mode aerosol fraction (f_f) values on the AOD leads to uncertainties in the retrieved total AOD. The magnitude of this uncertainty depends on the aerosol mode radii, refractive indices, wavelength, and it grows with the aerosol volume fraction, f_V. Typical f_V values for both maritime and urban areas are about $f_V \sim 2 \cdot 10^{-11}$ [22,26]. In our simulations, we used a slightly larger value, i.e., $f_V = 3.448 \cdot 10^{-11}$, which lies between the two extreme values 0 and 10^{-10} of f_V and corresponds to the orange line in Fig. 6, and we evaluated the AOD ($\tau_a(\lambda = 340\,\text{nm})$ for $f_V = 3.448 \cdot 10^{-11}$. Table 2 shows the maximum uncertainty at this f_V value for the bimodal size distribution. For the bimodal size distributions at $f_V = 3.448 \cdot 10^{-11}$, the minimum AOD value, obtained for $f_f = 0$, was subtracted from the maximum AOD value, obtained for $f_f = 1$, in order to assess the maximum AOD uncertainty arising from using the assumed values for f_f and f_c. The result is shown as $\text{Bimodal}_{\text{max}}$ in Table 2. Also shown in Table 2 is an error assessment for $f_V = 3.448 \cdot 10^{-11}$ with $f_f = 0.5$ as minimum and $f_f = 0.8$ as maximum. The result, which is shown as $\text{Bimodal}_{\text{real}}$ in Table 2, is expected to represent a more realistic situation.

It is evident that the uncertainties arising from unknown aerosol mode fraction values can be significant, especially for a bimodal aerosol distribution with widely separated geometric mean radii of the two modes. The maximum uncertainties $\text{Bimodal}_{\text{max}}$ given in Table 2 are theoretical and can be reduced. For example, the aerosol size distribution in the atmosphere is rarely expected to be better represented by a uni-modal than by a bimodal distribution. Therefore, one should avoid using the extreme values for the mode fractions and thus reduce the uncertainty. The sensitivity of the AOD to the fine-mode fraction can be minimized if one knows the aerosol size distribution and the fine-mode fraction. As an example, NASA's AERONET (AErosol RObotic

Optics EXPRESS

Table 2. Maximum uncertainties ($\text{Bimodal}_{\text{max}}$) and realistic uncertainties ($\text{Bimodal}_{\text{real}}$) in AOD values at 340 nm corresponding to an aerosol volume fraction of $f_V = 3.448 \cdot 10^{-11}$ for the maritime and urban bimodal size distributions.

	AOD_{min}	AOD_{max}	ΔAOD
$\text{Bimodal}_{\text{max}}$	0.04047	0.9084	0.86793
$\text{Bimodal}_{\text{real}}$	0.43396	0.70344	0.26948

NETwork) is a global, ground-based remote sensing aerosol network with open, accessible data bases. Size distribution parameters, mode fraction values and other retrieval products are available in the AERONET database. In case this information is not available the uncertainty can be significantly reduced using values for several locations suggested in the literature [26–28].

7. Suitable instrumentation and application possibilities

The method described in this paper is flexible and can be applied to a variety of multi-channel irradiance meters. Here we will discuss (i) what the optimum wavelengths would be for atmospheric AOD measurements, and (ii) what type of instruments might be the best fit for the methodology described in this paper. To investigate the impact of atmospheric gaseous absorption, we performed a simulation with 1 nm resolution of the atmospheric irradiance transmittance $F^-_{\text{BOA}}(\lambda)/F^-_{\text{TOA}}(\lambda)$, where $F^-_{\text{BOA}}(\lambda)$ is the downward irradiance at the 'bottom-of-atmosphere, BOA', and $F^-_{\text{TOA}}(\lambda)$ is the downward irradiance at the 'top-of-atmosphere, TOA', for wavelengths between 280 and 1,000 nm. In this simulation, we used the US standard atmosphere with a black underlying surface (surface albedo = 0) and solar zenith angle $\theta_0 = 0°$. Figure 7 shows the irradiance transmittance at sea level for an aerosol- and cloud-free atmosphere.

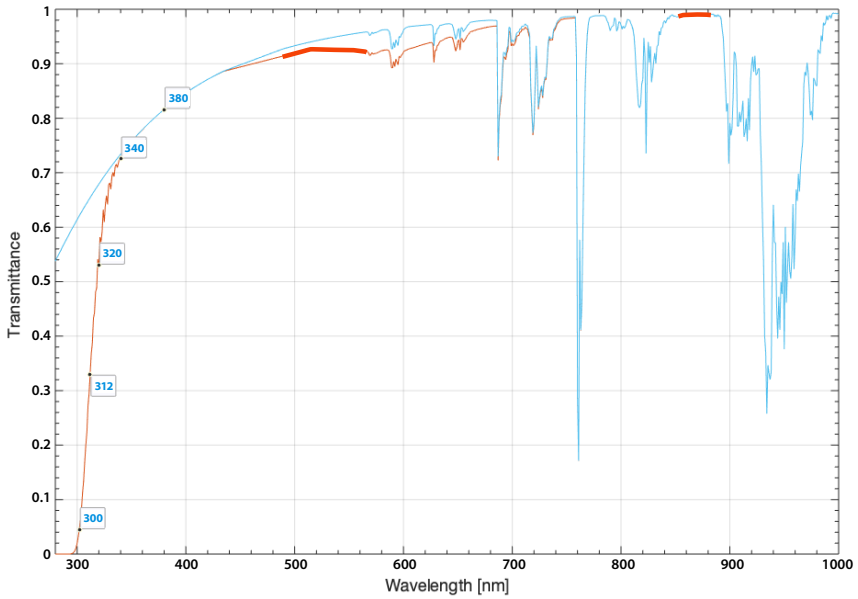

Fig. 7. Orange line: Atmospheric irradiance transmittance vs. wavelength for a clear (aerosol- and cloud-free) atmosphere. Blue line: Atmospheric irradiance transmittance vs. wavelength for a clear (aerosol- and cloud-free) atmosphere with zero ozone abundance. Red highlight: The spectral ranges between 488 and 566 nm as well as between 845 and 885 nm.

Optics EXPRESS

The impact of atmospheric gas absorption is clear in Fig. 7. An instrument with two channels at wavelengths with similar amounts of gaseous attenuation is a good choice for AOD measurements because absorption effects will cancel out when the ratio of the irradiances is taken, whereas the ratio of the irradiances at two different wavelengths is sufficiently sensitive to the AOD. In the flat spectral range in Fig. 7 between 488 and 566 nm (highlighted in red color) the transmittance varies by less than 0.0095%. This part of the spectrum lies within the Chappuis ozone absorption band (400 - 650 nm). An irradiance instrument with two channels in this spectral range simplifies the modeling calculations and minimizes the uncertainties. In the Chappuis band Rayleigh scattering is less dominant than at shorter wavelengths and ozone is responsible for the majority of the attenuation of light in the absence of aerosols and clouds. Figure 7 also indicates that the wavelength range between 845 and 885 nm (highlighted in red color) would be suitable for AOD retrieval, because gaseous absorption and Rayleigh scattering have minimal impact on the transmittance in this wavelength "window". In this spectral range the transmittance varies even less than in the 488 nm - 566 nm wavelength interval.

Based on the considerations above, an instrument with a channel at 500 nm and another channel at 550 nm would be suitable for AOD retrievals. Radiation measurements performed by ground-based or satellite-deployed instruments in the 500 nm wavelength range are most frequently used for AOD retrievals [29]. Figures 2 and 3 show simulated AOD values at 500 nm for maritime (coarse mode) and urban (fine mode) aerosol size distributions, respectively. Further, Fig. 3 shows that the AOD is less sensitive to the aerosol volume fraction at 500 nm than at 340 nm for urban type aerosols.

Table 3 shows the maximum AOD uncertainties (ΔAOD values) at $f_V = 3.448 \cdot 10^{-11}$ for a bimodal size distribution at wavelengths of 500 nm (500_{max}) and 870 nm (870_{max}) as well as error assessments (500_{real} and (870_{real}) associated with a more realistic scenario with $f_f = 0.5$ and $f_f = 0.8$ as minimum and maximum values. The maximum uncertainties (ΔAOD values) are defined as the difference between the AOD value for an atmosphere containing only fine-mode aerosols ($f_f = 1$) and the AOD value for an atmosphere containing only coarse-mode aerosols ($f_f = 0$). For the more realistic scenario the uncertainties are calculated as the difference of the AOD at $f_f = 0.5$ and $f_f = 0.8$.

Table 3. Minimum and maximum AOD values (AOD_{min} and AOD_{max}) and corresponding difference (ΔAOD) at 500 nm (500_{max}, second row) and at 870 nm (870_{max}, third row) for a bimodal size distribution.[a]

λ [nm]	AOD_{min}	AOD_{max}	ΔAOD
500_{max}	0.0446	0.4610	0.4164
870_{max}	0.05872	0.1467	0.08798
500_{real}	0.2082	0.33312	0.12492
870_{real}	0.04399	0.070384	0.02639

[a]Fourth and fifth rows show corresponding realistic values.

The NILU-UV instrument (see Sections 1 and 3) measures irradiance in five channels in the UV spectral range. These channels, centered at wavelengths 302 nm, 312 nm, 320 nm, 340 nm, and 380 nm, are indicated in Fig. 7. Originally, the NILU-UV instrument was designed to measure CIE-weighted UV dose rates, cloud effects, and the total ozone column amount. However, channel 4 (340 nm) and 5 (380 nm) measurements are barely sensitive to the total ozone column amount, and can be used to determine the AOD, as described in Section 8. The method to derive the total ozone column amount from NILU-UV measurements involves the ratio of either

Optics EXPRESS

$F(320\ \text{nm})/F(312\ \text{nm})$ or $F(320\ \text{nm})/F(302\ \text{nm})$; for details see [5,30]. Either one of these two channel pairs can be used to determine the total ozone column amount, and the channel ratio $F(340\ \text{nm})/F(380\ \text{nm})$ (see Fig. 5 and Section 8) can be used for simultaneous determination of the AOD, based on the method described in Section 4.

The total ozone column amount is also available from other sources, e.g., from NASA's Ozone Monitoring Instrument (OMI) deployed on the Aura satellite.

8. Demonstration

To test the algorithm described above for AOD retrieval, channel 4 (340 nm) and channel 5 (380 nm) of the NILU-UV instrument (number 115) will be used. At our measurement site, situated on the roof top of Stevens Institute of Technology, Department of Physics, Hoboken, NJ (latitude: 40.74° longitude: −74.03° altitude: ∼40 m) reliable measurements were available to test the algorithm. Each channel in the NILU-UV instrument includes an offset to account for the dark current of the detector and electrical offset in the amplifier (see, [31]). The instrument is equipped with moderate bandwidth filters that tend to drift with time. AccuRT was used to simulate irradiances for a clear, cloudless day at solar noon.

NILU-UV data collected on a cloudless day, October 2, 2010, will be used as an example. AccuRT was used to simulate irradiances at 340 nm and 380 nm for a range of aerosol fractions, f_V, at this day at solar noon, and the corresponding AOD value was obtained from AERONET. For the simulations the annual aerosol size distribution parameters, such as, $r_{\text{eff},n}$, σ_n, and f_f, were obtained from the AERONET database. In case AERONET data are not available, relevant information from the literature can also be used to approximate aerosol parameters for the time and location in question.

For each of the two channels, the raw data of the NILU-UV instrument were multiplied by a factor to make them equal to the simulated irradiances:

$$F_{\text{sim},4}(340\ \text{nm}) = c_4 \times V_4 \tag{11}$$

$$F_{\text{sim},5}(380\ \text{nm}) = c_5 \times V_5 \tag{12}$$

where $F_{\text{sim},4}(340\,\text{nm})$ and $F_{\text{sim},5}(380\,\text{nm})$ are simulated irradiances for channel 4 and 5, respectively, V_4 and V_5 are the collected raw data for channels 4 and 5, respectively, and the coefficients c_4 and c_5 are included to make the raw data agree with the simulated irradiances. The 340 nm and 380 nm channels of the NILU-UV were chosen because these channels are less influenced by ozone absorption than the other channels (302 nm, 312 nm, 320 nm). The shape of the spectrum does not vary much around 340 nm and 380 nm for variable atmospheric conditions or SZA. We accounted for the effective response due to the cosine response of the NILU-UV instrument by using the approach of [5], as explained below. The NILU-UV instrument has a flat diffuser and is designed to measure the downward irradiance (referred to as the ideal signal below)

$$F(\lambda, \theta_0) = \int_0^{2\pi} d\phi \int_0^{\pi/2} I(\lambda, \theta, \phi) \cos\theta \sin\theta d\theta \tag{13}$$

where $I(\lambda, \theta, \phi)$ is the radiance. The effective signal, $F^-_{\text{eff}}(\lambda, \theta_0)$ of the instrument is:

$$F_{\text{eff}}(\lambda, \theta_0) = \int_0^{2\pi} d\phi \int_0^{\pi/2} I(\lambda, \theta, \phi) Y(\theta, \phi) \cos\theta \sin\theta d\theta \tag{14}$$

where $Y(\theta, \phi)$ is the angular response function, which differs from the ideal cosine response and has a θ dependence that depends on atmospheric conditions. This type of angular response function is typical for flat diffusers [32,33]. In general, the more diffuse the radiation field, the smaller the variation in F^-_{eff}/F^- with the solar zenith angle. The ratio of the effective response

Optics EXPRESS

F^{-}_{eff} [Eq. (14)] and the ideal signal F^{-} [Eq. (13)] at 380 nm depends on the solar zenith angle θ_0 [see Section 2 of [5]] .

The uncorrected effective signal from channel i ($i = 4$ or $i = 5$) of the NILU-UV instrument is $F_{i,\text{eff}} = V_i \times c_i$ [see Eqs. (11) and (12)]. We are interested in the ratio R of the ideal signal in channel 4 to that in channel 5, i.e., $R = F_4/F_5$, which, in terms of $k_i(\theta_0) = F_{i,\text{eff}}/F_i$, can be written:

$$R = \frac{V_4 \times c_4 \times k_5(\theta_0)}{V_5 \times c_5 \times k_4(\theta_0)}. \tag{15}$$

The constants c_4 and c_5 were calculated from Eqs. (11) and (12) when $\frac{k_5(\theta_0)}{k_4(\theta_0)} = 1$. The $k(\theta_0)$ values were approximated based on Section 2 in [5].

Next, eleven clear-sky days were chosen for AOD retrieval. The clear-sky condition of each day was checked by plotting the raw data for channel 5 (380 nm), as illustrated in Fig. 8 for October 2, 2010.

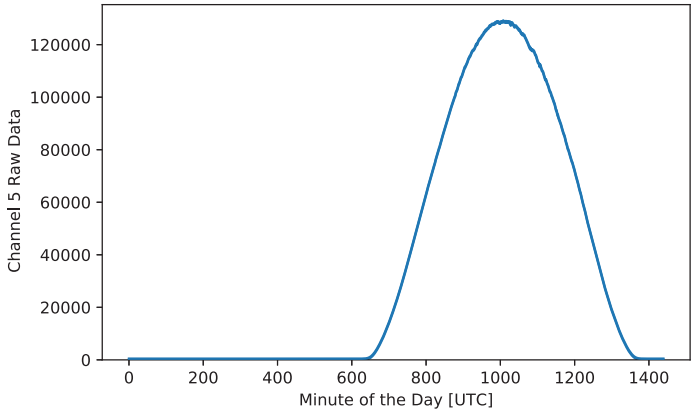

Fig. 8. Raw data of channel 5 on 10/02/2010 showing a cloudless day.

To construct an aerosol look-up table, we used yearly averages of aerosol data obtained for Year 2010 from the AERONET site at City College of New York, located at 40.82131° latitude and −73.94904° longitude at 100 m altitude, see Table 4.

Table 4. Yearly average aerosol parameters for 2010 derived from AERONET data collected at the City College of New York site.

$r_{\text{eff, f}}$ [μm]	$r_{\text{eff},c}$ [μm]	$r_{n,f}$ [μm]	$\sigma_{n,f}$	$r_{n,c}$ [μm]	$\sigma_{n,c}$	$f_{V,f}$
0.138740	2.109916	0.0864644	0.4349	0.6825431	0.6718	0.810

The parameters listed in Table 4 are the fine-mode effective radius ($r_{\text{eff},f}$), the course-mode effective radius ($r_{\text{eff},c}$), the fine-mode mean radius ($r_{n,f}$), the fine-mode standard deviation ($\sigma_{n,f}$), the coarse-mode mean radius ($r_{n,f}$), the coarse-mode standard deviation ($\sigma_{n,c}$), and the fine-mode volume fraction ($f_{V,f}$). AERONET provides the effective radii $r_{\text{eff},f}$ and $r_{\text{eff},c}$ of the fine and coarse modes, respectively. We calculated the mean radii of the fine and coarse modes using Eq. (6).

The complex refractive index values listed in Table 1 were used as described in Section 4. The solar zenith angles θ_0 were calculated at solar noon for the following eleven clear-sky days in 2010: 08/08 (day 220), 08/29 (day 221), 09/05 (day 252), 09/11 (day 258), 09/20 (day 267), 10/02 (day 279), 10/09 (day 286), 10/10 (day 287), 11/01 (day 308), 11/07 (day 314), 11/13 (day 320). The value of the ratio $F_{\text{sim},4}/F_{\text{sim},5}$ and the corresponding AOD and f_V values were provided in a look-up table at 600 equidistant points for every θ_0 value. Values of the ratio R,

Optics EXPRESS

calculated using Eq. (15) based on raw NILU-UV measurements were matched to the ratios in the synthetic database to retrieve values of f_V and AOD. Figure 9 shows retrieved solar-noon AOD values as well as daily average AOD values for the 11 days in 2010 listed above.

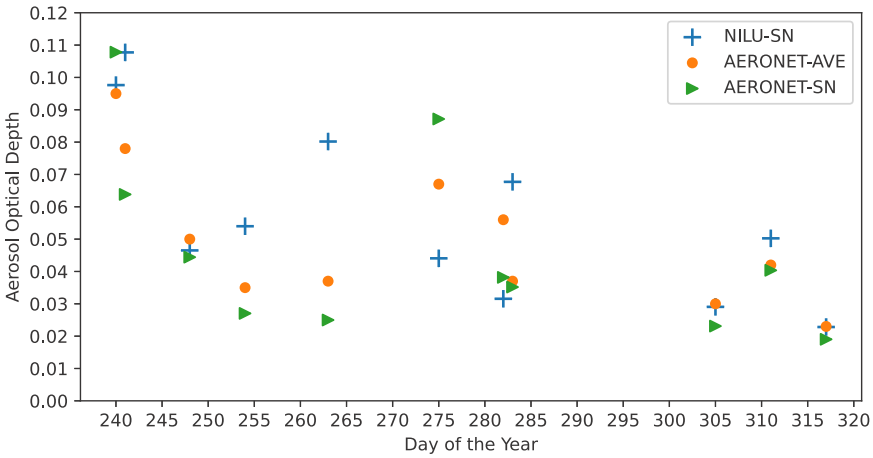

Fig. 9. AOD values in New York city area vs. day of the year in 2010 retrieved from the AERONET CCNY and NULI-UV measurement sites. Please note that the two locations are 10.80 km apart. Blue crosses: AOD values at 500 nm from NILU-UV retrievals at solar noon. Orange dots: Daily average AOD values from the AERONET City College of New York (CCNY) site. Green triangles: AOD values at solar noon from the AERONET CCNY site.

The AOD values in Fig. 9 and their temporal variation are typical for an urban coastal area, such as that where the NILU-UV measurements were taken and the AERONET observations were made. The AERONET products shown in Fig. 9 are solar noon values and daily averages, whereas the NILU-UV results were obtained at solar noon. Differences between the retrieved AOD values from the NILU-UV and AERONET measurements may arise due to local variation of the f_V values at such urban coastal areas. Other possible sources of retrieval errors may be the degradation of the NILU-UV instrument's Teflon diffuser, electronic background noise, the effective response of the detectors in different channels, and the use of yearly average aerosol microphysical and size distribution parameters when constructing the lookup-table.

9. Discussion

In general we can say that the AOD retrieval was successful using the method described in this paper. It assumes we have some knowledge about the aerosol size distribution parameters and indices of refraction as they need to be provided as an input. The aerosol microphysical and optical properties vary with time, location and season. The related parameters can be gathered from literature or other available data sources.

The flexibility of this method comes from the fact that the lookup-tables can be created for different atmospheric scenarios and the aerosol size distribution parameters and refractive indices can be set to match the aerosol features.

Previous work [34] has shown that cloud optical depth as well as TOC can be retrieved from irradiance data. In order to distinguish thin cloud from aerosol, an optical depth threshold could be established so that for optical depths below this threshold the observation is attributed to aerosol rather than cloud particles. Also, cloud particles are expected to have weaker dependence on wavelength than aerosol particles. Hence, the spectral shape of the measured irradiances could be used as another criterium to distinguish cloud from aerosol particles.

Optics EXPRESS

The AERONET and NILU-UV measurement sites are not co-located (they are 10.80 km apart with ~60 m altitude difference in a similar but slightly different environment) which can contribute to the differences in the retrieved AOD between the two instruments. Measurement errors may arise from the instruments' imperfect cosine response, calibration, atmospheric conditions and the sensitivity of the ratio described in Eq. (15).

10. Conclusion

AOD measurements are important for several reasons briefly described in Section 1. Our goal was to develop a simple, efficient, and easy to implement method for aerosol optical depth retrieval from multichannel irradiance measurements. An AOD retrieval algorithm has been described that can be used with ground or aircraft-deployed multichannel irradiance meters. The advantages of the method are: (i) it is designed for instruments with no moving parts, it is universally applicable for a variety of multi-channel irradiance meters, (ii) it provides retrieval of AOD values at multiple wavelengths simultaneously if needed.

The method is supported with model calculations, a proof of principle (Section 5), and verified in Section 8. Uncertainties are discussed in Section 6, and possible instrument configurations are described in Section 7. Ancillary data sources such as those described in Sections 6 and 8 can be used to significantly reduce the uncertainties as discussed in Section 6.

Finally, we should point out that (i) the lookup-tables constructed in this paper can be used for other cities that have similar geographical locations and atmospheric conditions (mid-latitude coastal cities with similar climate and aerosol composition), and (ii) seasonal lookup-tables can be used to improve the accuracy of retrieved AODs because seasonal changes are expected to lead to different aerosol composition and mode fractions.

Disclosures. The authors declare no conflicts of interest.

Data availability. Relevant parameters used for the simulations can be found in this article. Any further parameters, numerical values that were used are referenced in this article. NILU-UV data used in this research is available upon request from the corresponding author. All AERONET data used during this study is open to the public and available from the NASA-AERONET website [35].

References

1. K. Vohra, A. Vodonos, J. Schwartz, E. A. Marais, M. P. Sulprizio, and L. J. Mickley, "Global mortality from outdoor fine particle pollution generated by fossil fuel combustion: Results from GEOS-Chem," Environ. Res. **195**, 110754 (2021).
2. M. A. Kohanski, J. N. Palmer, and N. A. Cohen, "Aerosol or droplet: critical definitions in the COVID-19 era," Int Forum Allergy Rhinol. **10**(8), 968–969 (2020).
3. E. L. Anderson, P. Turnham, J. R. Griffin, and C. C. Clarke, "Consideration of the Aerosol Transmission for COVID-19 and Public Health," Risk Anal. **40**(5), 902–907 (2020).
4. N. Schutgens, A. M. Sayer, A. Heckel, *et al.*, "An AeroCom–AeroSat study: intercomparison of satellite AOD datasets for aerosol model evaluation," Atmos. Chem. Phys. **20**(21), 12431–12457 (2020).
5. B. A. K. Høiskar, R. Haugen, T. Danielsen, A. Kylling, K. Edvardsen, A. Dahlback, B. Johnsen, M. Blumthaler, and J. Schreder, "Multichannel moderate-bandwidth filter instrument for measurement of the ozone-column amount, cloud transmittance, and ultraviolet dose rates," Appl. Opt. **42**(18), 3472–3479 (2003).
6. B. Holben, T. Eck, I. Slutsker, D. Tanré, J. Buis, A. Setzer, E. Vermote, J. Reagan, Y. Kaufman, T. Nakajima, F. Lavenu, I. Jankowiak, and A. Smirnov, "AERONET - a federated instrument network and data archive for aerosol characterization," Remote Sensing of Environment **66**(1), 1–16 (1998).
7. T. Eck, B. Holben, J. S. Reid, O. Dubovik, A. Smirnov, N. T. O'Neill, I. Slutsker, and S. Kinne, "Wavelength dependence of the optical depth of biomass burning, urban, and desert dust aerosols," J. Geophys. Res.: Atmos. **104**(D24), 31333–31349 (1999).
8. O. Dubovik and M. D. King, "A flexible inversion algorithm for retrieval of aerosol optical properties from Sun and sky radiance measurements," J. Geophys. Res.: Atmos. **105**(D16), 20673–20696 (2000).
9. R. P. Lawson, B. A. Baker, C. G. Schmitt, and T. Jensen, "An overview of microphysical properties of Arctic clouds observed in May and July 1998 during FIRE ACE," J. Geophys. Res.: Atmos. **106**(D14), 14989–15014 (2001).
10. P. B. R. Peter Pilewskie, "Solar spectral flux, optical depth, and water vapor measurements and analyses in the Puerto Rico Dust Experiment (pride)," A Proposal to the Office of Naval Research, NASA (2000).

Optics EXPRESS

11. J. M. Haywood, S. R. Osborne, P. N. Francis, A. Keil, P. Formenti, M. O. Andreae, and P. H. Kaye, "The mean physical and optical properties of regional haze dominated by biomass burning aerosol measured from the C-130 aircraft during SAFARI 2000," J. Geophys. Res.: Atmos. **108**, (2003).
12. R. Arimoto, Y. Kim, Y. Kim, P. Quinn, T. Bates, T. Anderson, S. Gong, I. Uno, M. Chin, B. Huebert, A. Clarke, Y. Shinozuka, R. Weber, J. Anderson, S. Guazzotti, R. Sullivan, D. Sodeman, K. Prather, and I. Sokolik, "Characterization of Asian dust during ACE-Asia," Glob. Planet. Change **52**(1-4), 23–56 (2006).
13. S. C. Sherwood, P. Minnis, and M. McGill, "Deep convective cloud-top heights and their thermodynamic control during CRYSTAL-FACE," J. Geophys. Res.: Atmos. **109**(D20), D20119 (2004).
14. H. B. Singh, W. Brune, J. Crawford, D. J. Jacob, and P. Russell, "Overview of the summer 2004 intercontinental chemical transport experiment–north america (INTEX-A)," J. Geophys. Res.: Atmos. **111**(D24), D24S01 (2006).
15. R. Bergstrom, K. Schmidt, O. Coddington, P. Pilewskie, H. Guan, J. Livingston, J. Redemann, and P. Russell, "Aerosol spectral absorption in the Mexico City area: results from airborne measurements during MILAGRO/INTEX B," Atmos. Chem. Phys. **10**(13), 6333–6343 (2010).
16. D. D. Parrish, D. T. Allen, T. S. Bates, M. Estes, F. C. Fehsenfeld, G. Feingold, R. Ferrare, R. M. Hardesty, J. F. Meagher, J. W. Nielsen-Gammon, R. B. Pierce, T. B. Ryerson, J. H. Seinfeld, and E. J. Williams, "Overview of the second Texas air quality study (TexAQS II) and the Gulf of Mexico atmospheric composition and climate study (GoMACCS)," J. Geophys. Res.: Atmos. **114**, D00F13 (2009).
17. H. Jiang, G. Feingold, H. H. Jonsson, M.-L. Lu, P. Y. Chuang, R. C. Flagan, and J. H. Seinfeld, "Statistical comparison of properties of simulated and observed cumulus clouds in the vicinity of Houston during the Gulf of Mexico Atmospheric Composition and Climate Study (GoMACCS)," J. Geophys. Res.: Atmos. **113**(D13), D13205 (2008).
18. J. Huang, P. Minnis, B. Chen, Z. Huang, Z. Liu, Q. Zhao, Y. Yi, and J. K. Ayers, "Long-range transport and vertical structure of Asian dust from CALIPSO and surface measurements during PACDEX," J. Geophys. Res.: Atmos. **113**(D23), D23212 (2008).
19. B. Kindel, S. Schmidt, P. Pilewskie, S. Platnick, G. Wind, and A. Kokhanovsky, "Cloud radiative properties derived from the solar spectral flux radiometer (SSFR) during recent airborne field campaigns," in *AGU Fall Meeting Abstracts*, vol. 2008 (2008), pp. A11E–0191.
20. C. S. McNaughton, A. D. Clarke, S. Freitag, *et al.*, "Absorbing aerosol in the troposphere of the Western Arctic during the 2008 ARCTAS/ARCPAC airborne field campaigns," Atmos. Chem. Phys. **11**(15), 7561–7582 (2011).
21. T. B. Ryerson, A. E. Andrews, W. M. Angevine, *et al.*, "The 2010 california research at the nexus of air quality and climate change (CalNex) field study," J. Geophys. Res.: Atmos. **118**(11), 5830–5866 (2013).
22. K. Stamnes, B. Hamre, S. Stamnes, N. Chen, Y. Fan, W. Li, Z. Lin, and J. Stamnes, "Progress in forward-inverse modeling based on radiative transfer tools for coupled atmosphere-snow/ice-ocean systems: A review and description of the accurt model," Appl. Sci. **8**(12), 2682 (2018).
23. K. Stamnes and J. J. Stamnes, *Radiative Transfer in Coupled Environmental Systems: An Introduction to Forward and Inverse Modeling* (John Wiley & Sons, 2016).
24. Z. Ahmad, B. A. Franz, C. R. McClain, E. J. Kwiatkowska, J. Werdell, E. P. Shettle, and B. N. Holben, "New aerosol models for the retrieval of aerosol optical thickness and normalized water-leaving radiances from the SeaWiFS and MODIS sensors over coastal regions and open oceans," Appl. Opt. **49**(29), 5545 (2010).
25. H. Sugawara and T. Takamura, "Surface albedo in cities: case study in Sapporo and Tokyo, Japan," Boundary-Layer Meteorol. **153**(3), 539–553 (2014).
26. M. MacLeod, M. Scheringer, C. Götz, K. Hungerbühler, C. Davidson, and T. Holsen, *Deposition from the Atmosphere to Water and Soils with Aerosol Particles and Precipitation* (CRC Press, 2010).
27. P. Koepke, G. A. d'Almeida, and E. P. Shettle, *Atmospheric Aerosols - Global Climatology and Radiative Characteristics* (A. Deepak Publishing, 1991).
28. O. Dubovik, B. Holben, T. Eck, A. Smirnov, Y. Kaufman, M. King, D. Tanré, and I. Slutsker, "Variability of absorption and optical properties of key aerosol types observed in worldwide locations," J. Atmos. Sci. **59**(3), 590–608 (2002).
29. J. Xin, Y. Ma, R. Liu, L. Kong, L. Wang, Y. Ma, and W. Zhang, "Optimized broadband extinction method for retrieving 500 nm AOD with long-term direct solar radiation: Model test and application," Aerosol. Air Qual. Res. **17**(12), 3220–3229 (2017).
30. M. Sztipanov, L. Tumeh, W. Li, T. Svendby, A. Kylling, A. Dahlback, J. J. Stamnes, G. Hansen, and K. Stamnes, "Ground-based measurements of total ozone column amount with a multichannel moderate-bandwidth filter instrument at the troll research station, antarctica," Appl. Opt. **59**(1), 97–106 (2020).
31. NILU, "User's manual," (2008). Version 2.1.
32. J. Gröbner, M. Blumthaler, and W. Ambach, "Experimental investigation of spectral global irradiance measurement errors due to a non ideal cosine response," Geophys. Res. Lett. **23**(18), 2493–2496 (1996).
33. G. Bernhard and G. Seckmeyer, "New entrance optics for solar spectral UV measurements," Photochem. Photobiol. **65**(6), 923–930 (1997).
34. L. Fan, W. Li, A. Dahlback, J. J. Stamnes, S. Stamnes, and K. Stamnes, "New neural-network-based method to infer total ozone column amounts and cloud effects from multi-channel, moderate bandwidth filter instruments," Opt. Express **22**(16), 19595–19609 (2014).
35. "Aerosol robotic network (AERONET) Website," https://aeronet.gsfc.nasa.gov.